CellPress

Neuron
Article

# FLRT Structure: Balancing Repulsion and Cell Adhesion in Cortical and Vascular Development

Elena Seiradake,[1,7] Daniel del Toro,[2,7] Daniel Nagel,[2,5] Florian Cop,[3,4] Ricarda Härtl,[3,4] Tobias Ruff,[2] Gönül Seyit-Bremer,[2] Karl Harlos,[1] Ellen Clare Border,[1] Amparo Acker-Palmer,[3,4] E. Yvonne Jones,[1,*] and Rüdiger Klein[2,6,*]

[1]Division of Structural Biology, Wellcome Trust Centre for Human Genetics, University of Oxford, Roosevelt Drive, OX3 7BN Oxford, UK
[2]Max Planck Institute of Neurobiology, Am Klopferspitz 18, 82152 Martinsried, Germany
[3]Institute of Cell Biology and Neuroscience and Buchmann Institute for Molecular Life Sciences, Goethe University Frankfurt, Max-von-Laue-Str. 15, 60438 Frankfurt am Main, Germany
[4]Focus Program Translational Neurosciences, Johannes Gutenberg University Mainz, Saarstr. 21, 55122 Mainz, Germany
[5]Graduate School of Systemic Neurosciences, Ludwig-Maximilians-University Munich, Großhaderner Str. 2, 82152 Planegg-Martinsried, Germany
[6]Munich Cluster for Systems Neurology (SyNergy), 80336 Munich, Germany
[7]Co-first author
*Correspondence: yvonne@strubi.ox.ac.uk (E.Y.J.), rklein@neuro.mpg.de (R.K.)
http://dx.doi.org/10.1016/j.neuron.2014.10.008


## SUMMARY

**FLRTs are broadly expressed proteins with the unique property of acting as homophilic cell adhesion molecules and as heterophilic repulsive ligands of Unc5/Netrin receptors. How these functions direct cell behavior and the molecular mechanisms involved remain largely unclear. Here we use X-ray crystallography to reveal the distinct structural bases for FLRT-mediated cell adhesion and repulsion in neurons. We apply this knowledge to elucidate FLRT functions during cortical development. We show that FLRTs regulate both the radial migration of pyramidal neurons, as well as their tangential spread. Mechanistically, radial migration is controlled by repulsive FLRT2-Unc5D interactions, while spatial organization in the tangential axis involves adhesive FLRT-FLRT interactions. Further, we show that the fundamental mechanisms of FLRT adhesion and repulsion are conserved between neurons and vascular endothelial cells. Our results reveal FLRTs as powerful guidance factors with structurally encoded repulsive and adhesive surfaces.**

## INTRODUCTION

The development of complex tissues depends on a balance of intercellular adhesive and repulsive signaling. Cell adhesion provides spatial stability to nonmoving cells and traction for migrating cells (Solecki, 2012). Cell repulsion is the dominant mechanism for cell and axon segregation, tissue boundary formation, and topographic map formation (Dahmann et al., 2011; Klein and Kania, 2014). Several families of cell surface receptors, termed cell adhesion molecules (CAMs), provide homophilic (e.g., cadherins; Brasch et al., 2012; Cavallaro and Dejana, 2011) or heterophilic (e.g., integrins; Luo et al., 2007) cell-cell adhesive interactions. Members of the Netrin, semaphorin, slit, and ephrin families of cell guidance molecules act as cell-attached or secreted ligands, mediating repulsive or attractive/adhesive signaling via heterophilic interactions with cognate cell surface receptors (Bashaw and Klein, 2010; Kolodkin and Tessier-Lavigne, 2011). The fibronectin leucine-rich transmembrane proteins (FLRTs) are distinctive in sharing the characteristics of both functional groupings; they function as homophilic CAMs (Karaulanov et al., 2006; Maretto et al., 2008; Müller et al., 2011) and as heterophilic chemorepellents interacting with uncoordinated-5 (Unc5) receptors (Karaulanov et al., 2009; Yamagishi et al., 2011). Molecular-level insights into the mechanisms underlying these diverse modes of action are lacking, as is clarity on the contributions of adhesive versus repulsive activities to FLRT function in vivo.

The FLRTs (FLRT1–3) are regulators of early embryonic, vascular, and neural development (Egea et al., 2008; Leyva-Díaz et al., 2014; Maretto et al., 2008; Müller et al., 2011; O'Sullivan et al., 2012; Yamagishi et al., 2011). The homophilic and Unc5 interactions both involve the FLRT N-terminal leucine-rich repeat domain (LRR) (Karaulanov et al., 2006, 2009). This domain is followed by a linker region, a type 3 fibronectin domain (FN) and a juxtamembrane linker, which contains a metalloprotease cleavage site (Figure 1A). Proteolytic shedding of the FLRT2 ectodomain controls the migration of Unc5D-expressing neurons in the developing cortex (Yamagishi et al., 2011).

Like FLRTs, Unc5 receptors (Unc5A–D) are type 1 transmembrane proteins. The extracellular region contains two immunoglobulin-type domains (Ig1 and Ig2) and two thrombospondin-like domains (TSP1 and TSP2) (Figure 1A). Unc5 receptors act as classical dependence and repulsive signaling receptors for secreted Netrin ligands in the neural system (Lai Wing Sun et al., 2011). Netrin/Unc5B signaling also directs vascular development by controlling blood vessel sprouting (Larrivée et al., 2007). However, Netrin is not present in many Unc5-expressing tissues, for example, in the developing cortex, suggesting a dependence on other ligands.

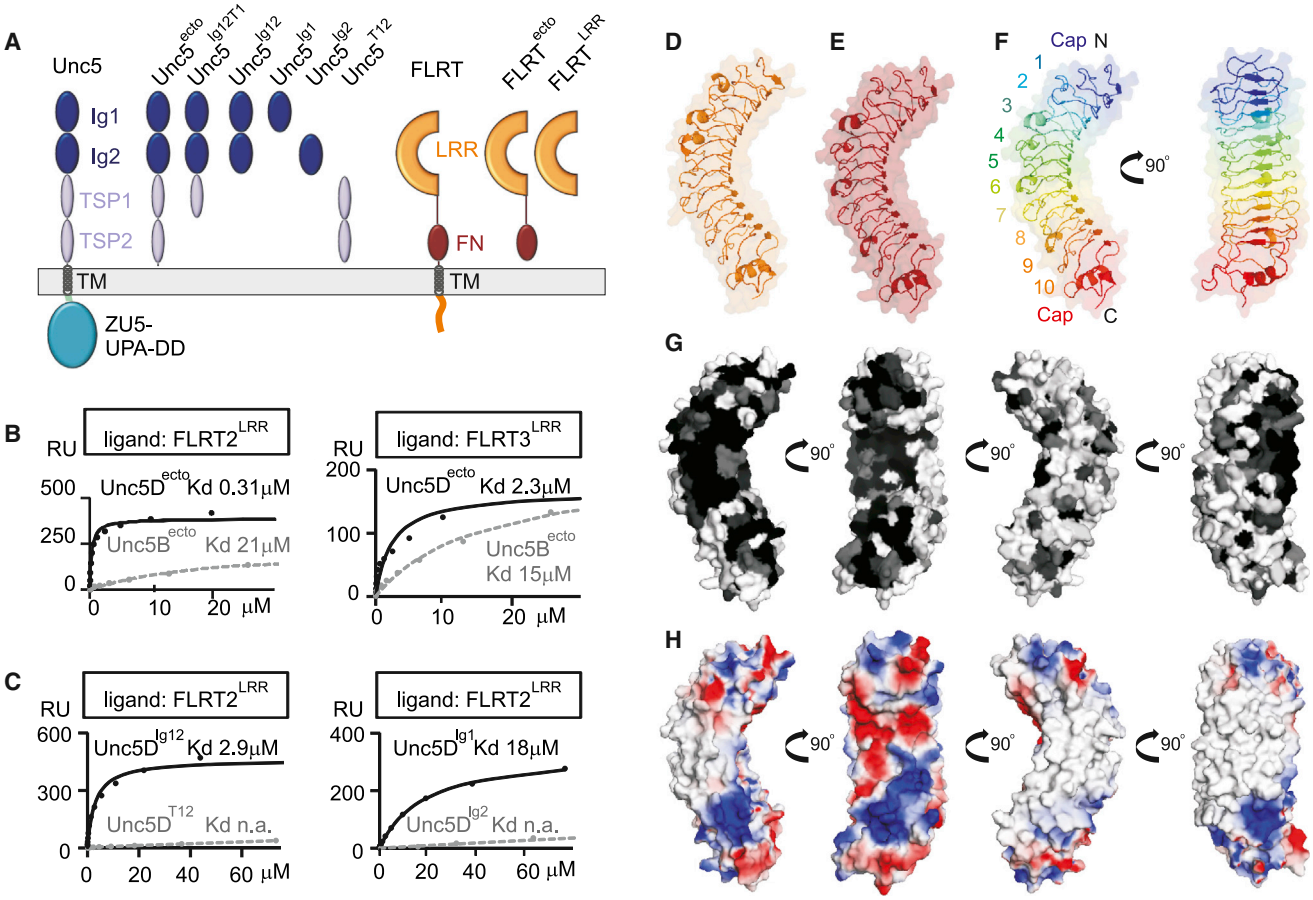


**Figure 1. SPR Experiments and Crystal Structures of FLRT$^{LRR}$ Proteins**

(A) Overview of *Flrt* and *Unc5* constructs used in SPR experiments. The intracellular region of Unc5 is composed of three domains: ZU5, UPA, and a death domain (DD) (Wang et al., 2009).

(B) We amine-coupled FLRT2$^{LRR}$ (left) or FLRT3$^{LRR}$ (right) on a CM5 chip and measured the binding of Unc5D$^{ecto}$ (black, solid lines) and Unc5B$^{ecto}$ (gray, dashed lines). Plotted are equilibrium response units (RU) at different analyte concentrations (μM). Curves were fitted and Kds calculated with a 1:1 binding model.

(C) As in (B), but measuring the binding of different Unc5D fragments to immobilized FLRT2$^{LRR}$.

(D) The crystal structure of FLRT2$^{LRR}$ is shown as a surface and ribbon diagram.

(E) FLRT3$^{LRR}$ is shown.

(F) FLRT3$^{LRR}$ colored according to the rainbow. Blue, N terminus; red, C terminus. The *lrr* motifs are numbered 1–10, and the positions of the cap structures are indicated.

(G) Surface views of FLRT3$^{LRR}$, colored according to sequence conservation within FLRT2/FLRT3 from mouse, fish, frog, and bird. Black, highest conservation; white, lowest conservation.

(H) Views of FLRT3$^{LRR}$ oriented as in (D), colored according to surface electrostatic surface potential (red, −69 kT/e; white, 0 kT/e; blue, +69 kT/e). k, Boltzmann's constant; T, temperature (310 K); e, $-1.6021766 \times 10^{-19}$ coulombs.

The dual functionality of FLRTs as CAMs that also elicit repulsion (as one of several possible Unc5 ligands) renders the analysis of their contributions in vivo challenging. Can cells integrate FLRT adhesive and repulsive signaling activities, and what are the contributions of these contradictory functionalities in different cellular contexts? To address the complexities of FLRT function we first sought to identify the structural determinants of the homophilic and heterophilic interactions.

Here we report crystal structures of FLRT2, FLRT3, Unc5A, Unc5D, and a FLRT2-Unc5D complex. Based on these data we assign homophilic adhesion and heterophilic repulsion to distinct molecular surfaces of FLRT. We show that by using these surfaces, FLRT can trigger both adhesive and repulsive signals in the same receiving cell, leading to an integrative response. Besides confirming that FLRT2/Unc5D repulsion regulates the radial migration of cortical neurons, we show here that FLRT3 also acts as a CAM in cortical development and modulates the tangential spread of pyramidal neurons. We further identify FLRT3 as a controlling factor in retinal vascularization. We demonstrate that FLRT controls the migration of human umbilical artery endothelial cells (HUAECs) through a similar mechanism to that which we found in the neuronal system. Taken together, our results reveal FLRT functions in cortical patterning and vascular development, and establish the FLRTs

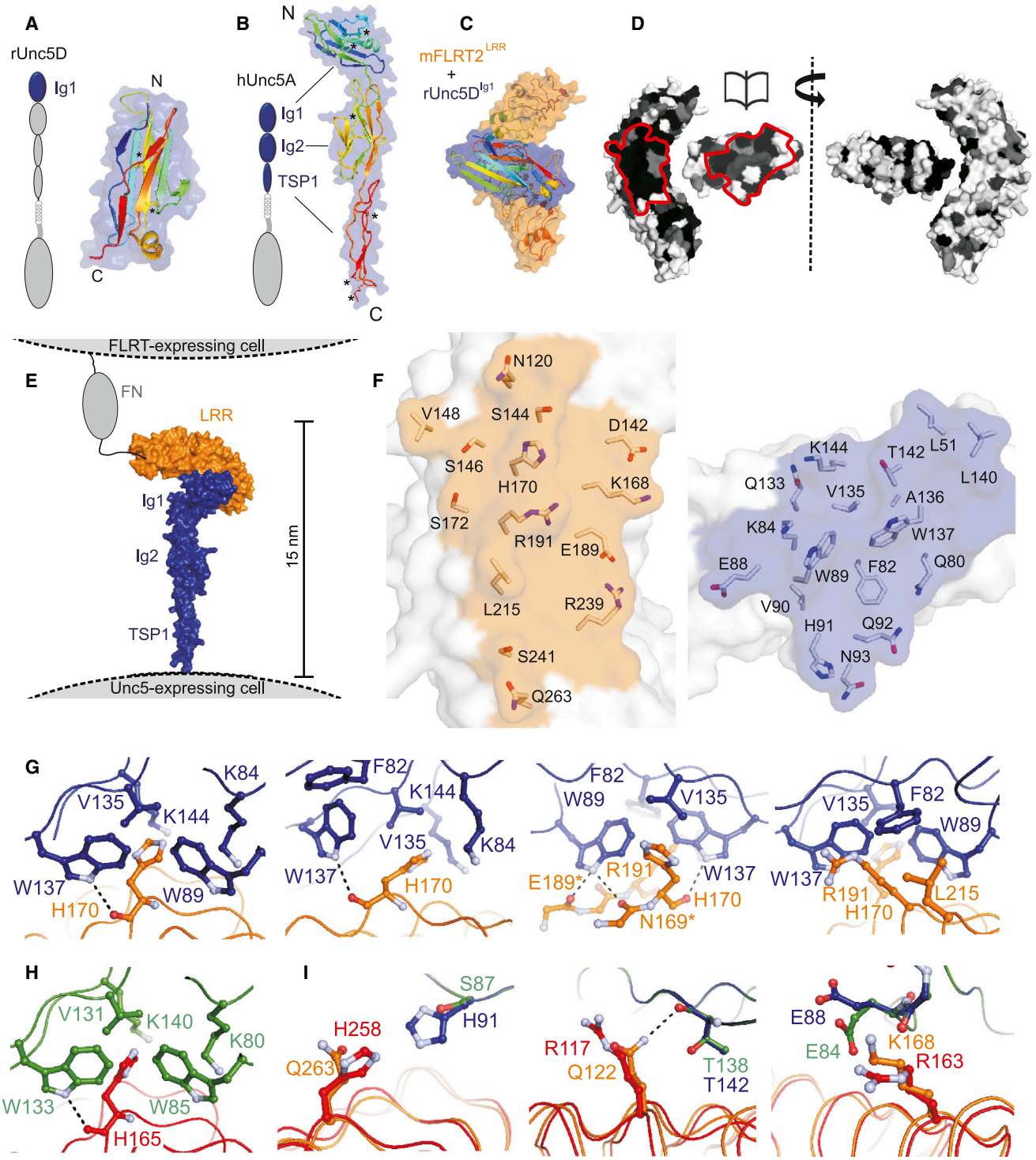


**Figure 2. Crystal Structures of Unc5 and a FLRT2-Unc5D Complex**

(A) The structure of Unc5D$^{Ig1}$ is shown as surface and rainbow ribbons (N terminus, blue; C terminus, red). Asterisks mark disulphide bridges.

(B) Structure of the complete human Unc5A ectodomain. Note that human Unc5A contains only one TSP domain. Asterisks mark disulphide bridges.

(C) Structure of FLRT2$^{LRR}$ (orange with rainbow ribbons) in complex with Unc5D$^{Ig1}$ (blue with rainbow ribbons).

(D) Left: view of FLRT2$^{LRR}$ and Unc5D$^{Ig1}$ as found in complex structure ("open book view"). Interacting surfaces are encircled in red. Surface colors represent sequence conservation within FLRT2/FLRT3 or Unc5B/Unc5D, respectively, from mouse, fish, frog, and bird. Black, highest conservation; white, lowest conservation. Right: FLRT2$^{LRR}$ and Unc5D$^{Ig1}$ rotated by 180° to reveal their less-conserved faces.

*(legend continued on next page)*

as a bimodal guidance system that combines homophilic adhesion with heterophilic repulsion.

## RESULTS

### Characterization of a High-Affinity Minimal FLRT-Unc5 Complex

We performed surface plasmon resonance (SPR) measurements using purified ectodomains of Unc5A, Unc5B, and Unc5D ($Unc5A^{ecto}$, $Unc5B^{ecto}$, $Unc5D^{ecto}$) and the LRR domains of their ligands FLRT2 and FLRT3 ($FLRT2^{LRR}$, $FLRT3^{LRR}$). These revealed a hierarchy of equilibrium dissociation constants (Kds), with the affinity of FLRT2 and Unc5D being the highest (Figure 1B; Table S1 available online). The relative affinities are consistent with those from previous cell-based binding assays (Karaulanov et al., 2009; Yamagishi et al., 2011), although the absolute values are lower, presumably due to differences in the techniques applied.

We also used SPR to test the binding of $FLRT2^{LRR}$ to Unc5D fragments encompassing different regions of the ectodomain ($Unc5D^{ecto}$, $Unc5D^{Ig12}$, $Unc5D^{Ig1}$, $Unc5D^{Ig2}$, and $Unc5D^{T12}$; depicted in Figure 1A). The results showed that the N-terminal Unc5D Ig domain ($Unc5D^{Ig1}$) harbors the major $FLRT2^{LRR}$-binding site (Figure 1C).

### Crystal Structures of $FLRT^{LRR}$ Reveal Conserved Surface Patches

We determined the crystal structures of mouse $FLRT2^{LRR}$ and $FLRT3^{LRR}$. Crystallographic details are provided in Table S2. Both structures consist of ten *lrr* repeats plus flanking cap structures, together forming a horseshoe-shaped solenoid (Figures 1D–1F, S1A, and S1B). Superposition underscores the similarity of the two structures with a root-mean-square deviation (rmsd) (Krissinel and Henrick, 2004) of 1.17 Å for 320 (out of 321) corresponding Cα atoms. We generated sequence conservation scores (Glaser et al., 2003) using alignments of FLRT2 and FLRT3 from mouse, chicken, frog, and fish and mapped these onto the $FLRT^{LRR}$ structures. A sequence-conserved patch extends from the concave to a lateral side surface of both $FLRT^{LRR}$ structures (Figures 1G and S1B). Comparison of $FLRT2^{LRR}$ with structures in the Dali database (Holm and Rosenström, 2010) shows strongest similarity (rmsd for 264 aligned Cα atoms = 1.8) with the cell adhesion protein decorin, which is known to dimerize via the concave surface of its LRR domain (Scott et al., 2004). The predominantly charged concave surfaces of $FLRT2^{LRR}$ and $FLRT3^{LRR}$ (Figures 1H and S1B) provide lattice contacts in all of our crystal structures (Figure S1), suggesting that these regions could mediate functional FLRT-FLRT interactions.

### A $FLRT2^{LRR}$-$Unc5D^{Ig1}$ Complex Reveals a Conserved Binding Interface

We determined the crystal structure of rat $Unc5D^{Ig1}$ (Table S2). The domain conforms to the Ig subtype 1 topology (Chothia and Jones, 1997) (Figure 2A). The structure is most similar to that of the N-terminal Ig domain of receptor protein tyrosine phosphatase delta (RPTPδ, rmsd for 86 aligned Cα atoms = 1.9 Å), although Unc5D lacks the positively charged surface patch that mediates the RPTPδ-glycosaminoglycan interaction (Coles et al., 2011).

We also solved a crystal structure for $Unc5A^{Ig12T2}$ (Table S2), thereby revealing the fold of the second Ig domain, also subtype 1, and the TSP domain (Figure 2B). The crystallized construct corresponds to the complete human Unc5A isoform 1 ectodomain. The overall structure is elongated and lacks extended interdomain linkers. All human Unc5A isoforms and mouse Unc5A isoform 2 lack the first of the two TSP domains that are present in other Unc5 homologs. Otherwise, the sequences of Unc5A–D are 44%–63% conserved between the human Unc5 homologs.

We solved the crystal structure of $FLRT2^{LRR}$ in complex with $Unc5D^{Ig1}$ (Table S2). Crystals diffracted to 4 Å only; however, the higher-resolution models of unliganded $FLRT2^{LRR}$ and $Unc5D^{Ig1}$ provide detailed information on the location of residues within each chain. $Unc5^{Ig1}$ binds to $FLRT2^{LRR}$ burying a total of ~1,280 $Å^2$ protein surface, which is highly sequence conserved on both sides (Figures 2C and 2D).

Superposition of $Unc5A^{Ig12T}$ with $Unc5D^{Ig1}$ as found in complex with $FLRT2^{LRR}$ generates a model in which the domains downstream of Unc5 Ig1 extend away from the interface with $FLRT^{LRR}$, suggesting that the Ig1 domain is the only interacting domain (Figure 2E). Based on this model alone, we cannot rule out that the extracellular FLRT regions downstream of the LRR domain also interact with Unc5. However, in SPR experiments we measured similar Unc5-binding affinities for $FLRT^{ecto}$ and $FLRT^{LRR}$ constructs (data not shown), suggesting that there is no major second Unc5-binding site on FLRT. We provide further support for this conclusion using a mutagenesis approach (see next section).

The core of the FLRT2-Unc5D-binding interface contains predominantly hydrophobic and positively charged residues (Figures 2F and 2G). The conserved FLRT2 histidine H170 forms a central anchor point that reaches deep into a hydrophobic pocket formed by Unc5D F82, K84, W89, V135, W137, and K144 and likely provides a hydrogen bond to Unc5D W137 (Figure 2G). FLRT2 R191 and L215 may stabilize this arrangement by providing additional contacts to Unc5D F82 and W137. The main residues forming the hydrophobic FLRT2-binding surface of Unc5D are fully conserved in Unc5B (Figure 2H), with the exception of F82, which is replaced by a tyrosine (Y78).

(E) The model of a FLRT-Unc5 complex between the surfaces of opposing cells was created by superposing Unc5A ectodomain (blue) on $Unc5D^{Ig1}$ as found in complex with $FLRT2^{LRR}$ (orange). Cell surfaces and FLRT2 regions that were not crystallized are depicted in gray.
(F) Residues within the interacting surfaces of FLRT2 (orange) and Unc5D (blue) are shown.
(G) Views of the interface between FLRT2 (orange) and Unc5D (blue). Selected residues are shown as sticks. Main chain stick atoms are not shown for all residues. Residues of which the main chain, but not the side chain, atoms are shown are marked with an asterisk. Putative hydrogen bonds are shown as dotted lines.
(H) View of FLRT-Unc5 interface residues as in (F), but showing the $FLRT3^{LRR}$ structure (red) and a homology model of $Unc5B^{Ig1}$ (green), in an arrangement based on the $FLRT2^{LRR}$-$Unc5D^{Ig1}$ structure.
(I) Views of interface residues that are not conserved between Unc5D/Unc5B (green/blue) and FLRT2/ FLRT3 (orange/red).

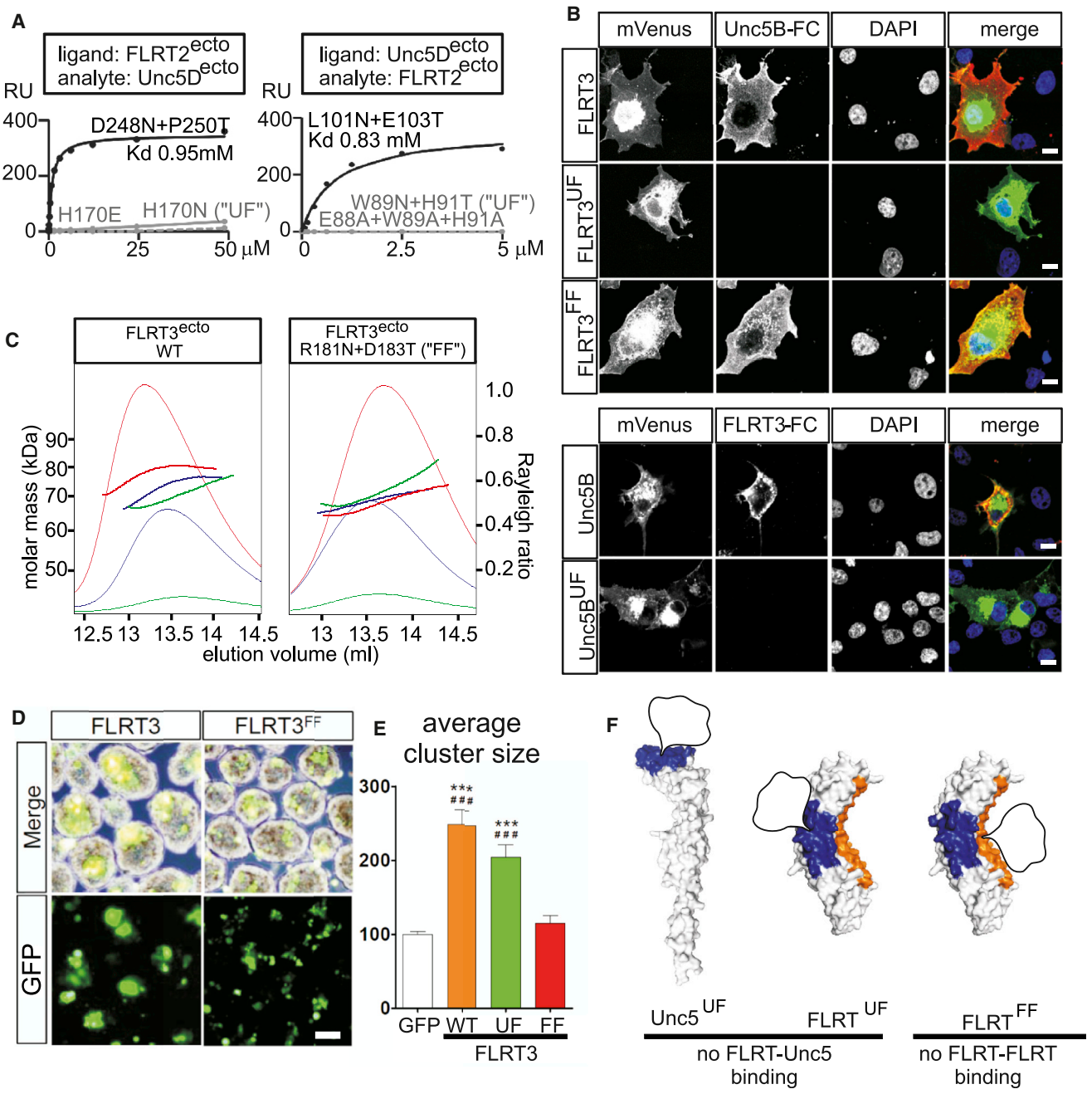


**Figure 3. Distinct Mutations Abolish FLRT-Unc5 and FLRT-FLRT Binding**

(A) SPR data showing that FLRT2 H170E or H170N and Unc5D W89N+H91T or E88A+W89A+H91A disrupt FLRT2-Unc5D binding. FLRT2 D248N+P250T and Unc5D L101N+E103T do not disrupt binding. The nonbinding mutants FLRT2 H170E and Unc5D W89N+H91T are henceforth denoted as "UF."

(B) We used an immunofluorescence-based binding assay (Yamagishi et al., 2011) to confirm mVenus-tagged FLRT3$^{UF}$ and Unc5B$^{UF}$ at the surface of cells do not bind Unc5B and FLRT3 ectodomains, respectively. Scale bars, 10 μm. Results for FLRT2 and Unc5D mutants are shown in Figure S2B.

(C) SEC-MALS experiments using wild-type FLRT3$^{ecto}$ and mutant proteins. Rayleigh ratios are depicted as thin lines (right axis). Protein concentrations at the peak maxima are ~0.1 mg/ml (green curves), ~0.5 mg/ml (blue curves), and ~1 mg/ml (red curves). Calculated masses are shown as thick lines (left axis). Multimerization leads to an increase in apparent molecular mass of wild-type FLRT3$^{ecto}$ at high concentrations, but not of the mutant FLRT3$^{ectoFF}$. Note that FLRT3$^{ectoUF}$ also multimerizes at high concentrations (Figure S2D).

(D) HEK cells transfected with control or *Flrt3* constructs (pCAGIG) were cultured in suspension. The average cluster size of transfected cells was measured and the results normalized to the GFP control. Scale bars, 40 μm. Data for FLRT2 are shown in Figures S2E and S2F.

*(legend continued on next page)*

The high degree of sequence conservation at the FLRT-Unc5-binding interface is in agreement with the observed binding promiscuity. Subtle differences in binding affinities for different homologs are likely due to sequence variations at the periphery of the binding interface (Figure 2I).

Histidine residues have a side chain $pKa_{(His)}$ of ~6, below which they are protonated. We predicted that the protonated FLRT2 H170 would be incompatible with binding to the hydrophobic binding pocket on Unc5D. Indeed, at pH ~5.7, $Unc5D^{ecto}$ does not interact with $FLRT2^{ecto}$ (Figure S2A).

## Mutations in the FLRT-Unc5 Interface Inhibit the Interaction

Based on the crystal structures, we designed mutations in the FLRT2-Unc5D interface to disrupt binding. In FLRT2 H170E and H170N, we replaced the central histidine with a negative-charged residue or an N-linked glycosylation site, respectively. Neither of these mutants binds Unc5D in our assays, confirming the binding site we describe is essential for the interaction (Figure 3A). Also, the Unc5D mutants E88A+W89A+H91A and W89N+H91T show poor binding to FLRT2 (Figure 3A). Binding was unaffected by FLRT2 and Unc5D mutations at sites involved in minor interactions in the crystal (FLRT2 D248N+P250T, Unc5D L101N+E103T), suggesting that these sites are not physiologically relevant (Figure 3A). For subsequent functional analysis we chose the non-Unc5-binding FLRT2 mutant H170N and the non-FLRT2-binding Unc5D mutant W89N+H91T. We henceforth refer to these Unc5-FLRT noninteracting mutants as $FLRT2^{UF}$ and $Unc5D^{UF}$, respectively. We confirmed our SPR results using a cell-based assay, in which we visualized the binding of soluble FC-tagged ectodomain proteins to mVenus-tagged receptors expressed on the surface of COS7 (Figure S2B).

The high degree of conservation in the Unc5-FLRT-binding sites allowed us to design binding-impaired mutants also for FLRT3 and Unc5B. We selected $FLRT2^{UF}$ and $Unc5D^{UF}$ as templates to design FLRT3 H165N ($FLRT3^{UF}$) and Unc5B W85N+S87T ($Unc5B^{UF}$) (Figure 3B). Additionally, we produced Unc5C W99N+H101T ($Unc5C^{UF}$), to test whether our mutants are valid also beyond the functionally well-characterized ligand/receptor pairs FLRT2-Unc5D and FLRT3-Unc5B. We showed that wild-type Unc5C, but not the UF mutant, is able to bind FLRT (Figure S2B). We confirmed that wild-type and mutant FLRT and Unc5 constructs are expressed at the cell surface (Figure S2C).

## FLRT-FLRT and Unc5-FLRT Interactions Are Mediated via Distinct Surfaces

Previous studies showed that FLRT-FLRT binding between cells is mediated via the LRR domain (Karaulanov et al., 2006). We were unable to detect $FLRT^{LRR}$-$FLRT^{LRR}$ binding using purified proteins in SPR experiments, possibly due to the low-affinity nature of the interaction. However, using size-exclusion chromatography coupled to multiangle light scattering (SEC-MALS), we could show that both $FLRT3^{ecto}$ and $FLRT3^{LRR}$ oligomerize in a concentration-dependent manner (Figures 3C and S2D). An increased population of FLRT dimers or oligomers at higher concentrations is detected as an apparent increase in molecular mass. We found that the calculated mass of $FLRT3^{ecto}$ and $FLRT3^{LRR}$ correlates with the protein concentration across the elution peak; the resulting "upside-down smiley" mass profile is typical for proteins undergoing concentration-dependent oligomerization.

Our crystal structures revealed that $FLRT^{LRR}$-$FLRT^{LRR}$ lattice contacts depend on the concave surface of the proteins, a region that mediates homophilic dimerization in other LRR proteins (Kajander et al., 2011; Scott et al., 2004, 2006; Seiradake et al., 2009). To probe this region, we produced the FLRT3 mutant R181N+D183T, which contains an N-linked glycosylation site in the concave surface. In contrast to wild-type $FLRT3^{ecto}$, the mutant does not undergo concentration-dependent oligomerization; i.e., the apparent mass does not increase in correlation with the protein concentration. These data show that the homophilic interaction depends on the concave surface of the FLRT3 LRR domain (Figure 3C). We henceforth call this FLRT-FLRT noninteracting mutation $FLRT^{FF}$, and the mutant ectodomain $FLRT3^{ectoFF}$. In contrast to $FLRT3^{ectoFF}$, the non-Unc5-binding mutant $FLRT3^{ectoUF}$ still oligomerizes in a concentration-dependent manner (Figure S2D).

We and others have shown that the expression of transmembrane FLRT in suspended HEK cells leads to the formation of separate cell aggregates (Egea et al., 2008; Karaulanov et al., 2006). Using this assay, we revealed that mutations in the concave surface of the FLRT3 LRR domain ($FLRT3^{FF}$), which disrupt FLRT3-FLRT3 ectodomain oligomerization in solution, also disrupt full-length FLRT3-based cell adhesion (Figure 3D). In contrast, FLRT3 with mutations in the convex surface of the LRR domain (S192N+P193G) and the Unc5-binding mutant $FLRT3^{UF}$ were still able to mediate cell adhesion (Figure 3E; data not shown). Based on our FLRT3 results, we designed an equivalent $FLRT2^{FF}$ mutant (R186N+D188T). The expression of FLRT2 and $FLRT2^{UF}$, but not $FLRT2^{FF}$, induced cell aggregation (Figures S2E and S2F). Thus, the FLRT-FLRT interaction surface we identified is conserved between the two homologs. We observed a small decrease in aggregation between cells expressing the UF mutants compared to wild-type FLRTs; however, the difference is not statistically significant. Western blot analysis confirmed similar expression levels of wild-type and mutant (Figure S2G). Finally, we demonstrated that $FLRT3^{FF}$ and $FLRT2^{FF}$ bind Unc5 ectodomains (Figures 3B and S2B). We conclude that FLRT-FLRT and FLRT-Unc5 interactions are mediated via distinct FLRT surfaces and can be controlled using specific mutations (Figure 3F).

## FLRTs Act as Chemo and Contact Repellents through Interaction with Unc5 in *trans*

We previously showed that shed ectodomains of FLRTs act as repulsive guidance cues and cause axonal growth cone collapse

(E) Quantification of the data shown in (D). $n \geq 3$ experiments per condition. $^{***}p < 0.001$ (versus GFP), $^{###}p < 0.001$ (versus FF), one-way ANOVA test with Tukey's post hoc analysis. The data are presented as mean ± SEM.

(F) The structures of $Unc5A^{ecto}$ (shades of blue) and $FLRT3^{LRR}$ (orange) are shown. To generate non-Unc5-FLRT-binding mutants $Unc5^{UF}$ and $FLRT^{UF}$ and the non-FLRT-FLRT-binding mutant $FLRT^{FF}$, we introduced N-linked glycosylation sites (schematized) in the respective binding sites.

of cortical neurons (Yamagishi et al., 2011). Here we use our specific FLRT mutant proteins to test whether this activity is solely dependent on FLRT-Unc5 interaction. We chose intermediate thalamic explants (iTh) expressing Unc5B (Figure 4A), the functional receptor of FLRT3. Using an automatic image analysis program (Figures S3A–S3C), we found that iTh growth cones collapse upon incubation with FLRT3$^{ecto}$ or FLRT3$^{ectoFF}$, compared to FC control protein. FLRT3$^{ectoUF}$ did not induce growth cone collapse, indicating that the collapse effect is dependent on FLRT3$^{ecto}$-Unc5 interaction (Figures 4B–4D). Similar results were obtained with a mixed culture of Unc5B/Unc5D-expressing cortical neurons stimulated with mutant or wild-type mixtures of FLRT2+FLRT3 (Figures S3D–S3G). We also performed stripe assays (Vielmetter et al., 1990) to test the responses of iTh axons toward different FLRT proteins. We found that iTh axons were repelled by stripes containing FLRT3$^{ecto}$ and FLRT3$^{ectoFF}$ (Figures 4E and 4F). iTh axons were also repelled by stripes presenting the non-Unc5-binding mutant FLRT3$^{ectoUF}$, but the effect was significantly less compared to the wild-type and FF mutant (Figures 4G and 4H). To investigate this further, we arranged alternating stripes presenting wild-type FLRT3$^{ecto}$ and the mutant FLRT3$^{ectoUF}$. iTh prefer to grow and extend axons on FLRT3$^{ectoUF}$, suggesting that the repulsive effect of FLRT3$^{ecto}$ is dependent, at least in part, on interaction with Unc5. Conversely, when asked to choose between the Unc5-binding competent FLRT3$^{ecto}$ and FLRT3$^{ectoFF}$ proteins, iTh axons do not show significant preference for either surface (Figures 4I–4K).

The stripe assay data raise the possibility that FLRT could also act as a surface-bound contact repellent. We confronted growing iTh axons with HeLa cells expressing a cleavage-resistant FLRT3 mutant, whose ectodomain is not shed (Yamagishi et al., 2011). Cells transfected with the noncleavable FLRT3 construct repelled ~80% of the extending axons, while non-transfected control cells repelled only ~20% of the axons (Figures 4L and 4M; Movies S1 and S2). Thus, FLRTs act as chemo and contact repellents, and this activity is largely mediated by Unc5 receptors.

## FLRT-FLRT Interaction Attenuates Unc5 Repulsion

During brain development, FLRTs and Unc5s are also expressed in overlapping regions. While iTh axons do not express detectable levels of FLRT3, rostral thalamic (rTh) axons express both Unc5B and FLRT3 (Figures 5A and 5B; Leyva-Díaz et al., 2014). We found that in stripe assays, rTh axons are repelled by FLRT3$^{ecto}$, but the effect is less pronounced compared to iTh axons. We also found that rTh axons from a *Flrt3* conditional mutant are repelled more strongly by FLRT3$^{ecto}$ stripes comparable to iTh axons lacking endogenous FLRT3 (Figures 5C–5E; see also Figure 4F). These data suggest that endogenous FLRT3 expressed on the axons modulates the response to FLRT3 presented (in *trans*) on stripes. Two scenarios could underlie this phenomenon: (a) FLRT3-FLRT3-mediated adhesion could counteract FLRT3-Unc5-mediated repulsion, or (b) FLRT3 could bind Unc5B in *cis*, thus reducing the number of Unc5B receptors that are able to respond to exogenous FLRT3 (“*cis* inhibition”). We performed stripe assays to explore this further. We found that rTh axons prefer to grow on wild-type FLRT3$^{ecto}$ rather than mutant FLRT3$^{ectoFF}$. rTh axons from a *Flrt3* conditional mutant do not distinguish between FLRT3$^{ecto}$ and FLRT3$^{ectoFF}$, thus behaving similar to iTh axons that naturally do not express FLRT3 (Figures 5F–5H; see also Figure 4K). These data suggest that the attenuation of repulsion observed for FLRT3-expressing neurons is due, at least in part, to adhesive FLRT3-FLRT3 interaction in *trans*. In stripe experiments where rTh axons choose between an inactive FLRT3 double mutant, containing both the FF and UF mutations (FLRT3$^{ectoFF-UF}$; Figure 5I) and FLRT3$^{ectoFF}$, rTh axons are repelled at least equally well by FLRT3$^{ectoFF}$ compared to iTh axons (Figures 5J–5L). These results argue that most, if not all, Unc5 receptors must be unmasked, despite the presence of endogenous FLRT3. Therefore, we conclude that in rTh axons FLRT3 and Unc5B function in parallel, such that adhesive FLRT interaction reduces the repulsive response triggered by FLRT-Unc5 interaction in a combinatorial way (Figure 5M).

## FLRTs Control Cell Migration in the Developing Cortex by Distinct Mechanisms

Having established how the adhesive and repulsive functions of FLRTs are mediated, we are now able to dissect these functionalities in vivo, using cortical development as a model system. During development, pyramidal neurons are born in the proliferative zone and radially migrate to settle in one of six cortical layers (Rakic, 1988). We previously showed that Unc5D-expressing neurons display a delayed migration to the FLRT2-enriched cortical plate consistent with FLRT2 acting as a repulsive cue for Unc5D+ cells (Yamagishi et al., 2011). Therefore, we wanted to investigate how much of the observed migration delay is due to FLRT-Unc5 signaling. In agreement with our previous work, we found that Unc5D overexpression by in utero electroporation (IUE) in E13.5-born neocortical cells delayed their migration. This delay was partially rescued when overexpressing Unc5D$^{UF}$ (Figures 6A–6C), confirming that the migration delay observed in Unc5D-overexpressing cells is at least partially due to interaction with FLRT2.

The pattern of FLRT3/Unc5B expression in E15.5 cortex is complementary to FLRT2/Unc5D, with FLRT3 expressed in migrating neurons and Unc5B in cortical plate (Figure 6D). To investigate whether FLRT3 plays a role in neuronal migration, we analyzed the positioning of neurons expressing FLRT3 in the developing cortex using brain sections from a *Nestin-Cre; Flrt3*$^{lox/lacZ}$ conditional mutant and β-galactosidase staining. We found that the distribution of FLRT3-deficient (β-gal+) neurons is affected in mutant cortex, leading to abnormal neuronal clustering in the cortical plate, which contrasts with the homogeneous distribution in control littermates (Figures 6E and 6F). To analyze the distribution of the β-galactosidase-positive neurons, we calculated the normalized intensity profile of the Xgal staining in the lower half of the cortical plate (dashed rectangle, Figures 6E and 6F), which revealed substantial fluctuations in the density of mutant neurons (Figure 6G). We also measured the Voronoi nearest neighbor distance to assess cellular distribution independently of cell density (Villar-Cerviño et al., 2013). Mutant neurons showed increased minimum distance between cells, which indicates that FLRT3 deletion affects the regular distribution present in control tissue (Figures S4A and S4B). This

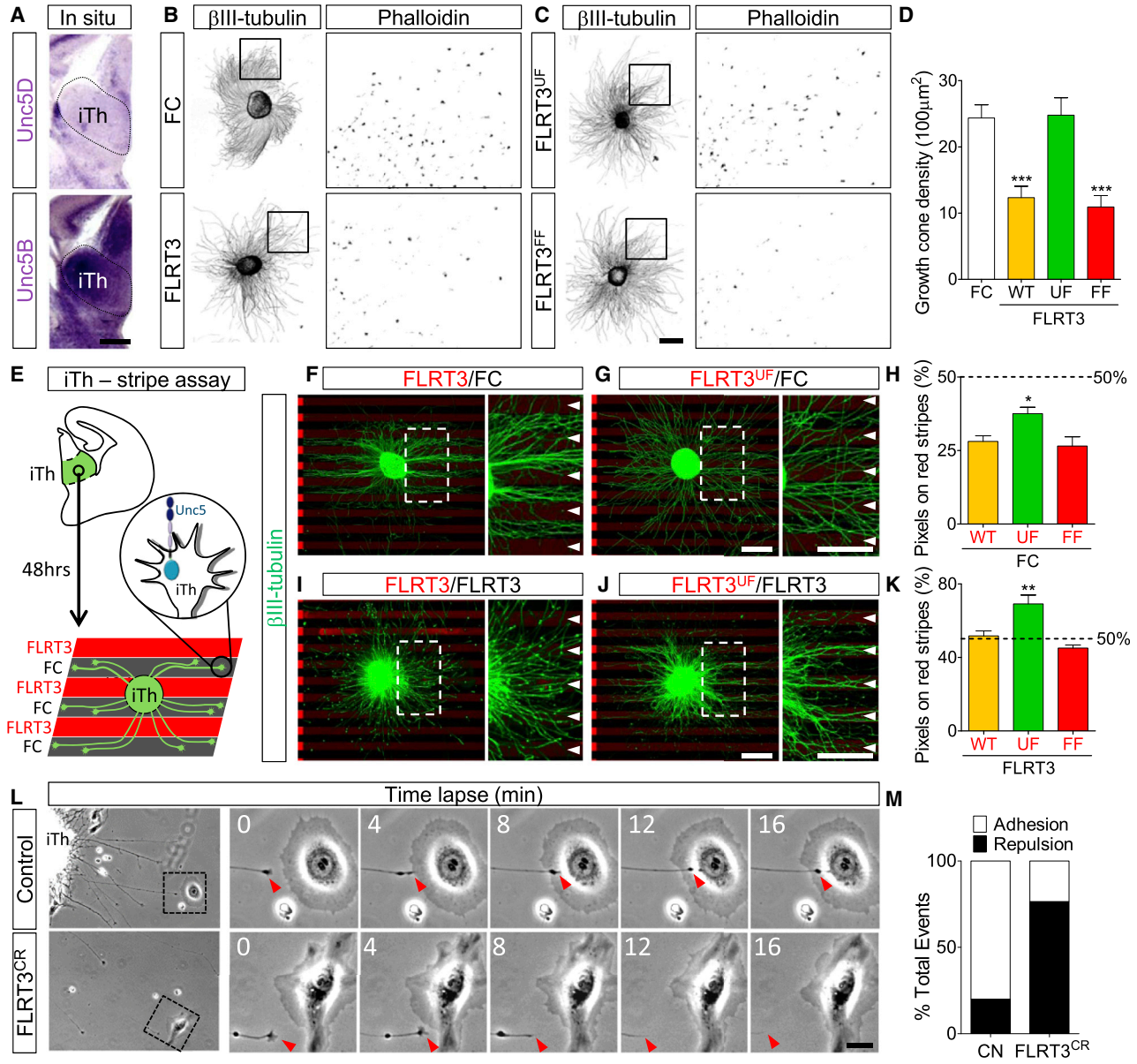


**Figure 4. FLRT-Unc5 Interaction in *trans* Induces Repulsion**

(A) In situ hybridization reveals *Unc5B* expression in the intermediate thalamus (iTh) of coronal sections through the telencephalon of E15.5 mouse embryos.

(B and C) iTh explants were treated with FLRT3$^{ecto}$, FLRT3$^{ectoFF}$, or FLRT3$^{ectoUF}$ fixed and stained with beta-III-tubulin and phalloidin.

(D) The density of growth cones in experiments shown in (B) and (C) was quantified as a measure to assess FLRT3-induced growth cone collapse. n ≥ 30 iTh explants per condition; ***p < 0.001, one-way ANOVA test with Tukey's post hoc analysis.

(E) Diagram depicting the stripe assay we used to probe the responses of iTh axons expressing Unc5B to surface-bound FLRT3 and FC control proteins.

(F and G) E15.5 iTh explants were grown on alternate stripes containing FC control protein or FLRT3$^{ecto}$ protein (wild-type or mutant). Explants were stained with anti-beta-III-tubulin to visualize the axons (green). FLRT3-containing stripes are marked in red on the left side of each image. After imaging, the percentage of beta-III-tubulin+ pixels on red stripes was quantified.

(H) Quantification of the data shown in (F) and (G). n ≥ 20 iTh explants per condition; *p < 0.05 (UF versus WT and FF), one-way ANOVA test with Tukey's post hoc analysis.

(I and J) Stripe assays were performed as described in (F) and (G), but using alternating stripes of wild-type and mutant FLRT3$^{ecto}$.

(K) Quantification of the data shown in (I) and (J). n ≥ 15 iTh explants per condition. **p < 0.01 (UF versus WT and FF), one-way ANOVA test with Tukey's post hoc analysis.

(L) Cell-bound FLRT3 repels iTh axons in time-lapse experiments. iTh explants were confronted with HeLa cells (control or expressing noncleavable FLRT3). Frames were acquired every 4 min. A repulsive event was defined as a contact between an extending axon and a HeLa cell lasting less than eight frames.

(M) Quantification of the data shown in (L); n ≥ 30 contacts per condition. The data are presented as mean ± SEM. Scale bars, 200 μm (A), 350 μm (B and C), 300 μm (F, G, I, and J), 13 μm (L).

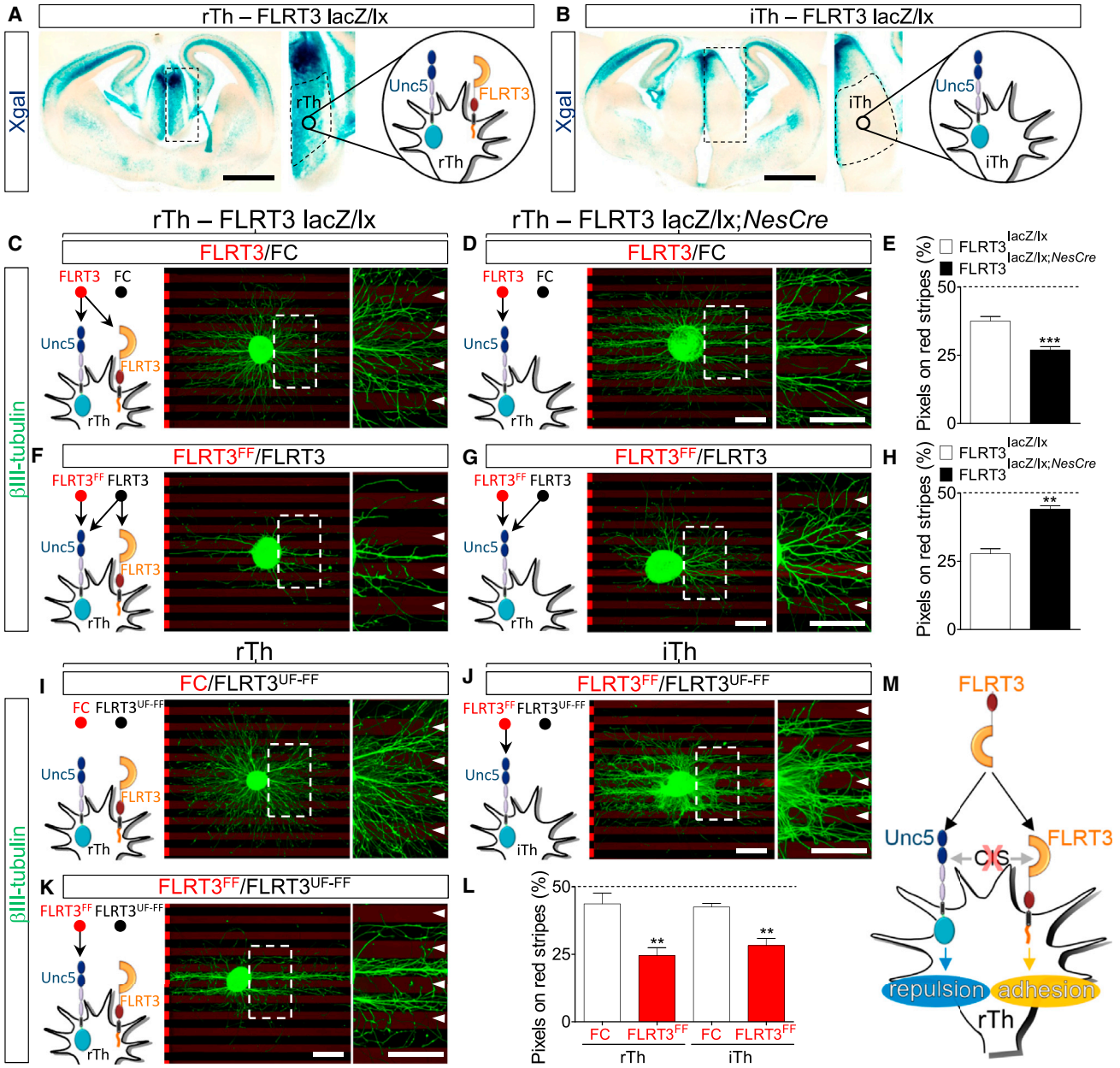


**Figure 5. FLRTs Act in *cis* as Attenuators of Unc5 Repulsion**

(A and B) Serial coronal sections through the telencephalon of E15.5 embryos from a *Flrt3*$^{lacZ/lx}$ reporter line showing high expression of *Flrt3* in rostral thalamus (rTh), but not intermediate thalamus (iTh).

(C and D) E15.5 wild-type or *Flrt3* conditional knockout rTh explants were grown on alternate stripes containing FC and FLRT3$^{ecto}$. Explants were stained with anti-beta-III-tubulin to visualize the axons (green). FLRT3-containing stripes are marked in red on the left side of each image. After imaging, the percentage of beta-III-tubulin+ pixels on red stripes was quantified.

(E) Quantification of the data shown in (C) and (D). n = 77 wild-type rTh from five embryos, n = 52 knockout rTh from six embryos. ***p < 0.001, two-tailed Student's t test.

(F and G) Stripe assays were performed as in (C) and (D), but using alternate stripes of FLRT3$^{ecto}$ and FLRT3$^{ectoFF}$.

(H) Quantification of the data shown in (F) and (G). n = 20 wild-type rTh from two embryos, n = 23 knockout rTh from three embryos. **p < 0.01, two-tailed Student's t test.

(I–K) rTh and iTh explants were grown on alternate stripes containing FC and FLRT3$^{ectoUF-FF}$, or FLRT3$^{ectoFF}$ and FLRT3$^{ectoUF-FF}$.

(L) Quantification of the data shown in (I) and (J). n ≥ 10 rTh and iTh explants per condition. **p < 0.01, two-tailed Student's t test.

(M) A model showing that FLRT-FLRT adhesion in *trans*, rather than FLRT-Unc5 interaction in *cis*, modulates FLRT-Unc5 repulsion in rTh axons. The data are presented as mean ± SEM. Scale bars, 850 μm (A and B), 300 μm (C, D, F, G, I, J, and K).

phenotype suggests that the normal tangential dispersion of cortical neurons is impaired in FLRT3 mutant mice. The radial positioning of pyramidal neurons seems unaffected; Cux1, a marker for upper-layer (Nieto et al., 2004), and TBR1, a marker of lower-layer, postmitotic neurons (Hevner et al., 2003), are expressed normally in FLRT3 mutant mice (Figures S4C–S4E). These results suggest that FLRT3 is required for the spatial arrangement of pyramidal neurons in the tangential axis. Mechanistically, this function of FLRT3 does not seem to involve interaction with Unc5B, since GFP-transfected migrating neurons show no preference between Unc5B$^{ecto}$-FC- and control FC-containing stripes (Figures 6H–6J). To obtain more insight into the mechanism of FLRT3 activity, we overexpressed the different mutants of FLRT3 in embryonic cortex using IUE. We analyzed transfected brains in cleared whole-mount preparations in both coronal and horizontal brain sections (Figure 6K). We found that FLRT3-overexpressing neurons migrate slower (Figures 6L and 6M) and distribute abnormally in the tangential axis, forming a repeating pattern of aggregates (Figures 6N, 6O, S4F, and S4G; Movies S3 and S4). Whereas the altered radial migration is not observed in the FLRT3 conditional mutants and may therefore be unphysiological, the altered tangential distribution is also seen when FLRT3 expression is ablated. FLRT3$^{UF}$ behaves similarly to wild-type FLRT3 and disrupts cell migration, and more importantly, tangential distribution of migrating neurons, suggesting that Unc5B does not affect the migration of FLRT3-expressing neurons (Figures 6L–6O, S4F, and S4G). Conversely, the mutation in FLRT3$^{FF}$ largely preserves the regular distribution of neurons in the tangential axis, indicating that FLRT-FLRT interaction is responsible for the observed effect (Figures 6L–6O, S4F, and S4G). FLRT3-overexpressing cells contain the differentiation marker Cux1, implying that FLRT3 affects the migration, but not differentiation, of the cells (Figures 6P and 6Q). Our results show that FLRTs have distinct functions in cortical development, mediating repulsion to control radial migration and homophilic adhesion to direct tangential distribution (Figures 6R and 6S).

### FLRT3 Controls Retinal Vascularization

FLRT and Unc5 proteins are expressed broadly during development, not just in the nervous system. FLRTs have been previously implicated in heart and vascular development (Müller et al., 2011), and artery endothelial cells are known to express Unc5B (Larrivée et al., 2007; Lu et al., 2004; Navankasattusas et al., 2008). We tested whether FLRT-Unc5 interaction plays a role in directing vascular cells. We found that primary HUAECs express both FLRT3 and Unc5B (Figure 7A). Stripe assays reveal that HUAECs are repelled strongly by FLRT3$^{ecto}$ compared to the FLRT3$^{ectoUF}$ mutant (Figures 7B and 7C). Conversely, the mutant FLRT3$^{ectoFF}$, which is unable to provide FLRT-FLRT adhesion, but still binds Unc5, is more repulsive than wild-type FLRT3 (Figures 7B–7E). As shown above for rTh neuronal axons (Figure 5), the data suggest that the response of HUAECs to FLRT3-presenting stripes is a product of adhesive FLRT-FLRT and repulsive FLRT-Unc5 interaction.

Next, we tested whether FLRT-Unc5 interaction plays a role in the developing vascular system. The mouse retina is an established model tissue for vascularization and, from birth until P8/P9, contains high levels of Unc5B in retinal arteries, capillaries, and endothelial tip cells (Larrivée et al., 2007). We found that FLRT3 is expressed in the inner plexiform layer of the retina during the stages when Unc5-expressing blood vessels develop (Figure 7F). To study the role of FLRT-FLRT and FLRT-Unc5 interactions in tip cell filopodia extension, we used live-mounted retinal explants (age P5). After incubation with FLRT3$^{ecto}$ or FLRT3$^{ectoFF}$, we measured significantly fewer tip cell filopodia at the vascular front compared to control and FLRT3$^{ectoUF}$ retinas (Figures 7G and 7H). Consistent with FLRT3-Unc5B repulsive interaction having a function during vascularization in vivo, we observed increased vascular branching in the retinas of *Sox2-Cre;Flrt3*$^{lox/lacZ}$ conditional mutants (Figures 7I and 7J). These data indicate that FLRT3 acts as a controlling factor of retinal vascular development and suggests that the action of FLRT3 depends on its interaction with Unc5B.

## DISCUSSION

The structural data presented here indicate that distinct FLRT LRR surfaces mediate homophilic adhesion and Unc5-dependent repulsion. By using these surfaces, FLRTs can affect both adhesive and repulsive functions in the same receiving cell, e.g., neurons or vascular cells that coexpress FLRT and Unc5. We show that coexpressed FLRT and Unc5 act in parallel, and that cells must integrate these adhesive and repulsive effects. This separation of adhesive and repulsive functionalities allows FLRTs to regulate the behavior of migrating pyramidal neurons in distinct ways; FLRT2 repels Unc5D+ neurons and thereby controls their radial migration, while FLRT3-FLRT3 homophilic interactions regulate their tangential distribution. FLRT3 also controls retinal vascularization, possibly involving combinatorial signaling via FLRT and Unc5. To distinguish FLRTs from adhesion-only CAMs, we propose to define a new subgroup, here designated as repelling CAMs (reCAMs). reCAMs provide a guidance system that combines the finely tunable cell adhesion of classical homophilic CAMs with repulsive functions through the addition of a heterophilic receptor.

### FLRT-FLRT and Unc5-FLRT Interaction Surfaces Are Distinct

We show here that FLRT-mediated adhesion involves the conserved concave surface on the LRR domain. This mode of homophilic binding resembles that of other LRR-type CAMs, for example, decorin (Scott et al., 2004). The FLRT-FLRT binding affinity is weak (below the sensitivity of our SPR assay ~100 μM), and FLRT oligomerization correlates with local concentration. Thus, FLRTs are ideal candidates for providing the finely tuned adhesive cell-cell traction required for cell migration.

In contrast to the low-affinity adhesive binding, repulsive FLRT-Unc5 interaction is of nanomolar affinity and mediated through a distinct binding surface on the FLRT LRR domain. The high degree of conservation within the binding surfaces of Unc5 and FLRT homologs suggests the interaction evolved before homolog diversification. The mode of interaction is atypical for LRR-type proteins, which mostly bind ligands via the concave surface of the domain, although some examples of ligand-binding surfaces other than the concave side exist (Bella et al., 2008).

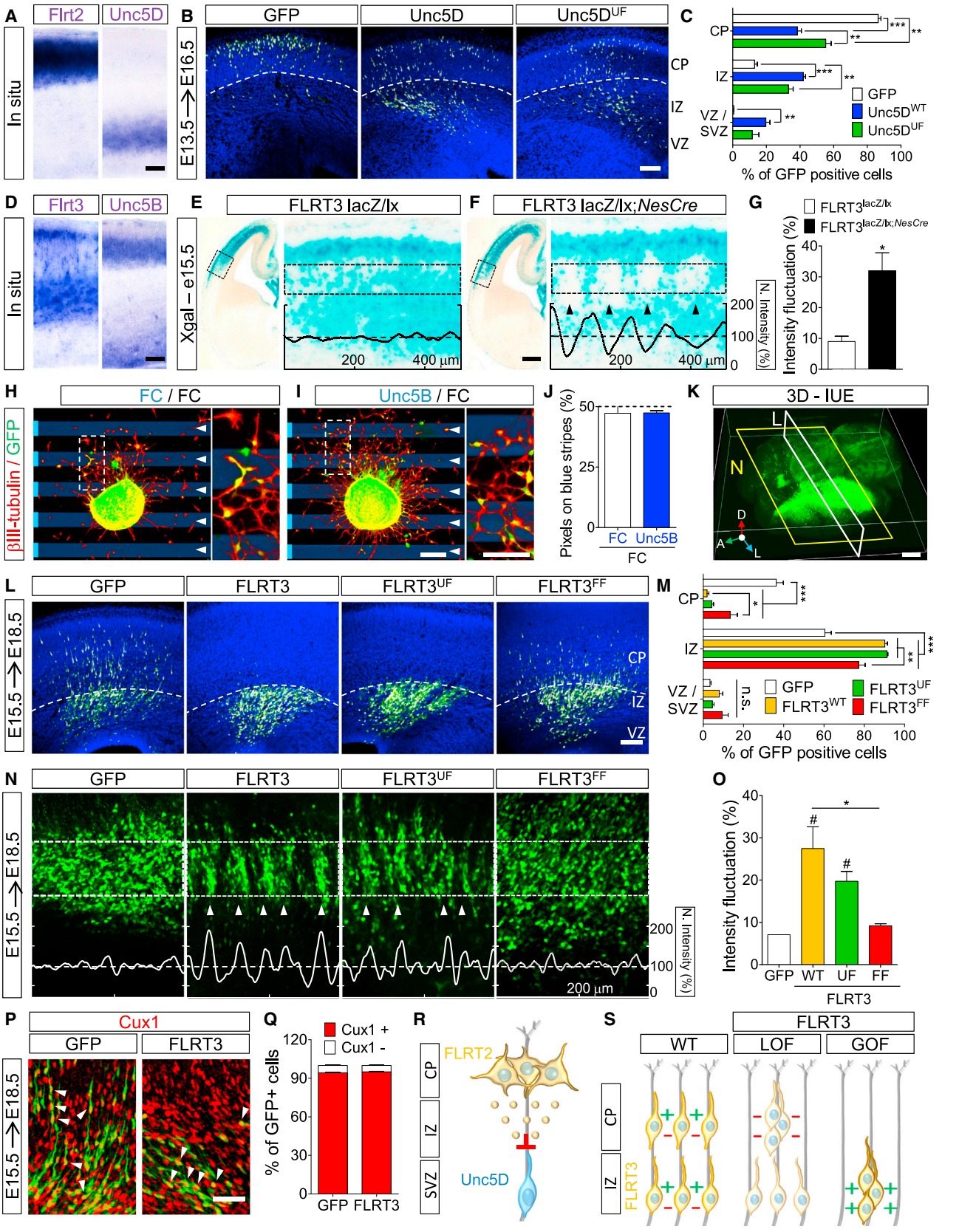


*(legend on next page)*

Our results with thalamic neurons and vascular cells indicate that coexpressed FLRTs act as attenuators of Unc5 repulsion. Stripe assays with FLRT3-positive, compared to FLRT3-negative, thalamic axons provide strong evidence that the attenuation results from FLRT-FLRT interaction in *trans*, rather than in *cis*, masking. Further work will be necessary to elucidate the functional consequences of this parallel signaling and the relative importance of membrane-associated versus soluble FLRT ectodomains in vivo.

## FLRTs Control Cortical Neuron Migration by Distinct Mechanisms

The mammalian cerebral cortex is organized in horizontal layers and intersecting columns. During development, cortical progenitors and their neuronal progeny settle in different layers in an inside-out fashion. The layered structure of the cortex helps to organize cortical inputs and outputs. Cortical progenitors and their neuronal progeny also form vertical ontogenic columns of sister neurons. Subpopulations of clonally related neurons undergo limited tangential dispersion to neighboring columns (Rakic, 1988). The molecular mechanisms and significance of this behavior are poorly understood. We have previously shown that FLRT2/Unc5D signaling is implicated in the radial migration of cortical neurons (Yamagishi et al., 2011). The FLRT2 ectodomain produced and shed by cells in the cortical plate prevents Unc5D+ cells from prematurely migrating from the subventricular zone to the cortical plate. In support of this model, Unc5D overexpression in E13.5-born neocortical cells further delayed their migration (this study and Yamagishi et al., 2011). Using the non-FLRT-binding mutant Unc5D$^{UF}$, we now confirm that this effect is at least partially due to FLRT/Unc5D interactions.

Our present results suggest that the related FLRT3 protein is implicated in the tangential dispersion of cortical neurons in a manner that involves FLRT3-FLRT3 homophilic interactions. The irregular distribution of cortical neurons in *Flrt3* mutant mice resembles the phenotype seen in *ephrinA* triple-knockout mice (Torii et al., 2009). Likewise, the tangential clustering of neurons after FLRT3 overexpression resembles the phenotype seen after EphA7 or ephrinB1 overexpression (Dimidschstein et al., 2013; Torii et al., 2009). The function of Eph/ephrin signaling appears to modulate cell morphology and mobility during the multipolar phase of migration (Dimidschstein et al., 2013). Based on its molecular functions, we hypothesize that FLRT3 affects the adhesive properties of migrating cells and thereby disrupts the delicate balance of adhesion/repulsion necessary for cell migration (Cooper, 2013; Marquardt et al., 2005; Solecki, 2012). This conclusion is supported by the fact that the non-FLRT-interacting mutant FLRT3$^{FF}$ is not able to disrupt the tangential dispersion. Interestingly, this function of FLRT3 may be shared by the related FLRT1 that is coexpressed with FLRT3 in the developing cortex and displays similar characteristics in terms of homophilic and Unc5 binding (Yamagishi et al., 2011; data not shown). A preliminary characterization of *Flrt1;Flrt3* double-knockout mutants revealed a stronger spatial disruption in the tangential axis of the cortex than single *Flrt3* mutants (data not shown). Together, these findings shed light on the cell-cell communication mechanisms operating during radial and tangential patterns of migration of pyramidal neurons.

## FLRT3 Controls Vascularization

Unc5B is a negative regulator of developmental vascularization (Bouvrée et al., 2008; Koch et al., 2011; Larrivée et al., 2007;

**Figure 6. FLRT Controls Radial and Lateral Migration of Cortical Neurons via Distinct Mechanisms**

(A) In situ hybridization shows *Flrt2* and *Unc5D* expression in coronal sections of E15.5 cortex.

(B) Coronal sections of E16.5 cortex after IUE at E13.5 with *GFP*, *Unc5D-IRES-GFP*, or *Unc5D*$^{UF}$*-IRES-GFP*. GFP+ cells located in the cortical plate (CP), intermediate zone (IZ), and subventricular zone (SVZ) were quantified.

(C) Quantification of the data shown in (B). n $\geq$ 5 electroporated embryos per condition. **p < 0.01, ***p < 0.001, one-way ANOVA test with Bonferroni post hoc analysis.

(D) In situ hybridization shows *Flrt3* and *Unc5B* expression in coronal sections of E15.5 cortex.

(E and F) Xgal staining of E15.5 coronal sections from control (*Flrt3*$^{lacZ/lx}$) or conditional (*Flrt3*$^{lacZ/lx;NesCre}$) mutant. Normalized intensity plots are shown, obtained from the areas delineated with a dashed rectangle.

(G) Quantification of the intensity fluctuations by measuring the distances between minima and maxima and the normalized intensity values (dashed line). n = 3 controls, n = 4 conditional mutants. *p < 0.05, two-tailed Student's t test.

(H and I) GFP-electroporated cortical explants (from E13.5 to E15.5) were plated on alternating stripes coated with FC control protein or Unc5B$^{ecto}$-FC fusion. Explants were stained with anti-beta-III-tubulin to visualize neurons exiting the explant (red). After imaging, the percentage of GFP+ pixels on blue stripes was quantified.

(J) Quantification of the data shown in (H) and (I). n $\geq$ 7 cortical explants per condition.

(K) Cleared whole-mount electroporated brain (E15.5–E18.5) showing the orientation of sections presented in (L) (coronal) and (N) (horizontal).

(L) Coronal sections of E18.5 cortex after IUE at E15.5 with *GFP*, *Flrt3-IRES-GFP*, *Flrt3*$^{UF}$*-IRES-GFP*, and *Flrt3*$^{FF}$*-IRES-GFP*. GFP+ cells located in the CP, IZ, and SVZ were quantified.

(M) Quantification of the data shown in (L). n $\geq$ 5 electroporated embryos per condition. *p < 0.05, **p < 0.01, ***p < 0.001, statistical analysis as in (C).

(N) As in (L), but showing horizontal optical sections from a cleared whole-mounted electroporated brain.

(O) Quantification as described for (G), but for data shown in (N). n $\geq$ 3 electroporated embryos per condition. *p < 0.05, one-way ANOVA test with Tukey's post hoc analysis and #p < 0.05 (WT and UF versus FF), two-tailed Student's t test.

(P) Staining of electroporated slices (*GFP* or *Flrt3-IRES-GFP*) with the laminar marker Cux1 (red).

(Q) Quantification of the data shown in (P). n $\geq$ 3 electroporated embryos per condition.

(R) Cartoon depicting how FLRT2, expressed and shed in the cortical plate, delays the migration of Unc5D+ neurons located in the SVZ.

(S) Cartoon depicting how FLRT3 directs cortical neuron migration. In the WT, the lateral distribution of neurons is controlled by a correct balance of adhesive and repulsive interactions. FLRT3 knockdown (LOF) or overexpression (GOF) alters this balance, resulting in the formation of neuronal cell clusters. The data are presented as mean ± SEM. Scale bars, 400 μm (A and D), 250 μm (E and F), 150 μm (B and L), 300 μm (H and I), 1 mm (K), 100 μm (P).

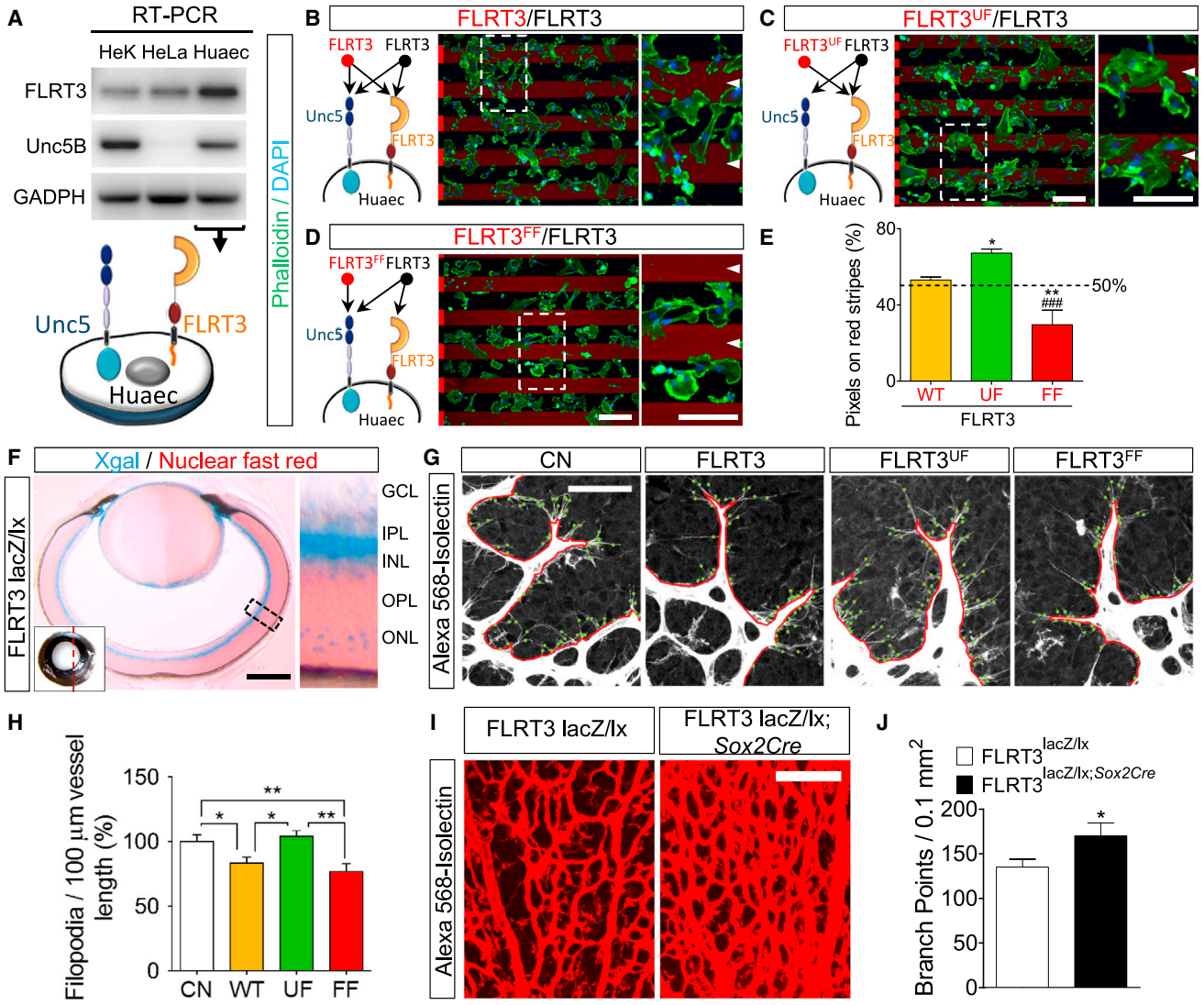


**Figure 7. FLRT Controls Vascular Development via Conserved Mechanisms**

(A) RT-PCR data showing that HUAECs express *Flrt3* and *Unc5B*.

(B–D) HUAECs were grown on alternate stripes containing wild-type and mutant FLRT3$^{ecto}$. Cells were stained with phalloidin (green) and DAPI (blue). The location of the faintly stained red stripes is indicated on the left side of each image.

(E) After imaging, the percentage of DAPI+ pixels on red stripes was quantified. HUAECs are attracted to FLRT3$^{ectoUF}$ stripes and repelled by FLRT3$^{ectoFF}$ stripes, when FLRT3$^{ecto}$ is present on the control stripes (black). n $\geq$ 2 cultures made in duplicate. *p < 0.05, **p < 0.01 (versus WT), and ###p < 0.001 (versus UF), one-way ANOVA test with Tukey's post hoc analysis.

(F) Longitudinal section through the eye of a P2 mouse from an *Flrt3*$^{lacZ/lx}$ reporter line showing expression of *Flrt3* in the inner plexiform layer and outer nuclear layer, counterstained with FastRed. GCL, ganglion cell layer; IPL, inner plexiform layer; INL, inner nuclear layer; OPL, outer plexiform layer; ONL, outer nuclear layer.

(G) P5 retinal explants were incubated with wild-type FLRT3, mutant FLRT3$^{UF}$, or FLRT3$^{FF}$ protein for 4 hr. The number of tip cell filopodia at the vascular front was quantified.

(H) Quantification of data shown in (G). n = 3–9. *p < 0.05, **p < 0.01, one-way ANOVA test with Tukey's post hoc analysis.

(I) The branch points in the retinal vasculature from control (*Flrt3*$^{lacZ/lx}$) or conditional (*Flrt3*$^{lacZ/lx;Sox2Cre}$) mutant (P3) were quantified.

(J) Quantification of data shown in (I). n = 4–8. *p < 0.05, two-tailed Student's t test. The data are presented as mean ± SEM. Scale bars, 90 µm (A), 300 µm (F), 50 µm (G), 100 µm (I).

Lu et al., 2004), and Unc5B knockdown leads to increased vascular branching in the mouse retina (Koch et al., 2011). Netrin-1 and Robo-4 have been shown to interact with Unc5B in the vasculature (Koch et al., 2011; Lu et al., 2004); however, neither *Netrin1*$^{-/-}$ nor *Robo4*$^{-/-}$ mice display the hypervascularization effects observed in *Unc5B*$^{-/-}$ retinas, indicating that

other factors may play a role. Here we demonstrate that *Flrt3*$^{-/-}$ mice present with a vascularization phenotype that strongly resembles that reported for Unc5B$^{-/-}$. Using our tip cell collapse experiments, we show that soluble FLRT3 controls the extension of endothelial tip cell filopodia through its specific Unc5B-binding site, providing functional evidence for a direct interaction of FLRT3 and Unc5. These results suggest that FLRT3 is a major player in controlling vascularization via Unc5B, and may therefore explain the puzzling lack of effects in retinal vascularization after removing other Unc5B ligands. Our stripe assays showed that surface-tethered FLRT3 also repels endothelial cells through interaction with Unc5B. Further work is required to understand whether FLRT3 acts in its soluble or cell-bound form in vivo.

Further questions remain; how do FLRTs signal adhesion/attraction in response to homotypic interaction with other FLRTs? Are the downstream pathways activated by the FLRT intracellular domain similar to classical CAMs? Are small GTPases such as Rnd proteins (Chen et al., 2009; Karaulanov et al., 2009) and cytoskeletal proteins involved? FLRTs have also been reported to bind other proteins, for example, latrophilin (O'Sullivan et al., 2012). It will be important to understand the molecular determinants of these interactions and how they influence FLRT functions. The crosstalk of FLRT3-Unc5B interactions to other key vascular players, such as VEGF/VEGFR2, also remains to be investigated.

In summary, we integrated information generated by a broad range of biological methods to understand the functions of FLRT and Unc5 receptors in cortical and vascular development. Our results reveal how FLRTs act as bimodal guidance molecules directing essential developmental processes through structurally distinct, combinatorial mechanisms. As FLRT and Unc5 are expressed in a wide range of tissues (Engelkamp, 2002; Haines et al., 2006), the conserved functional mechanisms we report are likely to control cell adhesion and repulsion in tissues beyond those described here.

## EXPERIMENTAL PROCEDURES

### Vectors and Cloning

We cloned constructs of mouse *Flrt2* (UniProt Q8BLU) and *Flrt3* (UniProt Q8BGT1), human *Unc5A* (UniProt Q6ZN44), mouse or human *Unc5B* (UniProt Q8K1S3 and Q8IZJ1), and rat *Unc5D* (UniProt F1LW30) into the Age1-Kpn1 or EcoR1-Kpn1 cloning site of vectors from the pHLSec family (Aricescu et al., 2006), depending on whether the construct includes a native secretion signal sequence. For crystallization or functional analysis, we cloned *Flrt2*$^{LRR}$ (residues 35–362), *Flrt3*$^{LRR}$ (residues 29–359), *Flrt2*$^{ecto}$ (residues 35–540), *Flrt3*$^{ecto}$ (residues 29–526), *Unc5A*$^{Ig12T1}$ (residues 1–303), human *Unc5B*$^{ecto}$ (residues 1–375), *Unc5D*$^{Ig1}$ (residues 1–161), *Unc5D*$^{Ig12}$ (residues 1–244), *Unc5D*$^{T12}$ (residues 249–382), and *Unc5D*$^{ecto}$ (residues 1–382) into pHLSec vectors containing short C-terminal tags (poly-His or poly-His+avitag; see Aricescu et al., 2006). For visualization in cells, we cloned full-length *Flrt2* (residues 35–660), *Flrt3* (residues 29–649), *Unc5B* (residues 27–934), *Unc5C* (residues 41–931), and *Unc5D* (residues 46–953) into a pHLSec vector that codes for a C-terminal mVenus and a polyhistidine tag (Seiradake et al., 2010). Hemagglutinin epitope (HA) tags are included at the N terminus of transmembrane constructs, following the vector secretion signal sequence. For expression in vivo, we subcloned *Flrt* and *Unc5* constructs with the pHLSec vector signal sequence and HA tag into a pCAGIG vector coding for a C-terminal internal ribosome entry site (IRES) and GFP. We generated point mutants using standard PCR techniques. We verified the correct cell surface expression of all transmembrane plasmids by immunostaining (Figure S2C; data not shown).

### Protein Purification, Crystallization, and Data Collection

We expressed FLRT and Unc5 ectodomain proteins destined for crystallization or functional analysis transiently in GnTI-deficient HEK293S cells or HEK293T cells (Aricescu et al., 2006), respectively, and purified the proteins using Ni-affinity and size-exclusion chromatography. Prior to crystallization, we added recombinant endoglycosidase F1 (Chang et al., 2007) at a concentration of 0.01 mg/ml to all samples. Crystals were grown by the vapor diffusion method at 20°C by mixing protein and crystallization solutions in a 1:1 (v/v) ratio. See Supplemental Experimental Procedures for crystallization solutions. We collected X-ray diffraction images at the Diamond Light Source beamlines I03, I04, and I24 and processed data using XDS (Kabsch, 1993), xia2 (Winter et al., 2013), and programs from the Collaborative Computational Project 4. In brief, the structure of Unc5D$^{Ig1}$ was solved by the single anomalous diffraction method. All other structures were solved by molecular replacement. See the Supplemental Experimental Procedures.

### SPR

We performed equilibrium experiments using a Biacore T200 machine (GE Healthcare) at 25°C. The experiments were carried out at pH 7.5 (PBS, 0.005% [v/v] polysorbate 20), unless indicated otherwise. Experiments at pH 5.7 were run in 150 mM NaCl and 50 mM citric acid. The regeneration buffer was 2 cM $MgCl_2$. To mimic the native membrane insertion topology, we biotinylated proteins enzymatically at the C-terminal avidity tag and attached the resulting biotin label to streptavidin-coated Biacore chip surfaces. Data were analyzed with Scrubber2 (BioLogic). $K_d$ and maximum analyte binding ($B_{max}$) values were obtained by nonlinear curve fitting of a 1:1 Langmuir interaction model (bound = $B_{max}/(K_d c+cC)$, where $C$ is analyte concentration calculated as monomer).

### Multiangle Light Scattering

We purified protein samples by size-exclusion chromatography and concentrated to 1–10 mg/ml. Separation for MALS was achieved using an analytical Superdex S200 10/30 column (GE Heathcare), and the eluate was passed through online static light scattering (DAWN HELEOS II, Wyatt Technology), differential refractive index (Optilab rEX, Wyatt Technology), and Agilent 1200 UV detectors (Agilent Technologies). We analyzed data using the ASTRA software package (Wyatt Technology).

### Stripe Assay, Growth Cone Collapse, Cell Aggregation, Cell-Binding Assay, IUE, Cleared Whole-Mount Brains, Retinal Explants Culture, and Immunostaining

These assays were performed as described previously (Calegari et al., 2004; Chung and Deisseroth, 2013; Sawamiphak et al., 2010; Yamagishi et al., 2011). See also the Supplemental Experimental Procedures.

### Mouse Lines

*Flrt3*$^{lacZ/lx}$ mice (Egea et al., 2008) carrying the floxed allele for *Flrt3* were crossed with the nervous system-specific *Nestin-Cre* (Tronche et al., 1999) or *Sox2-Cre* line (Hayashi et al., 2002). All animal experiments were approved by the government of upper Bavaria.

## ACCESSION NUMBERS

The wwPDB accession numbers for the crystal structures reported in this paper are 4v2a (hUnc5A ectodomain), 4v2b (rUnc5D Ig1 domain), 4v2c (complex of rUnc5D Ig1 and mFLRT2 LRR domains), 4v2d (mFLRT2 LRR domain), and 4v2e (mFLRT3 LRR domain).

## SUPPLEMENTAL INFORMATION

Supplemental Information includes four figures, two tables, four movies, and Supplemental Experimental Procedures and can be found with this article online at http://dx.doi.org/10.1016/j.neuron.2014.10.008.

## AUTHOR CONTRIBUTIONS

E.S. led crystallography, mutagenesis, SPR, and MALS and assisted stripe/collapse assays. D.d.T. led assays with HUAECs, neuronal cultures/explants, mutant brain sections, and IUE. D.N. led cell-based binding assays and analyzed IUE experiments, T.R. cleared and analyzed IUE brains, and G.S.-B. led HEK aggregation assays. F.C. and R.H. lead tip cell collapse assays and mutant retina analysis. T.R. performed whole-mounted cleared brain studies. K.H. assisted crystal freezing. E.C.B. produced $FLRT3^{LRR}$ for MALS assays. The above and A.A.P., E.Y.J., and R.K. contributed to discussions and manuscript preparation.

## ACKNOWLEDGMENTS

We thank E. Robertson, E. Bikoff, M. Harkiolaki, and A.R. Aricescu for *Flrt* constructs and discussion; Y. Zhao and W. Lu for protein expression; M. Jones and T.S. Walter for technical support; the Diamond Light Source for beamtime (proposal mx8423); and the staff of beamlines I03, I04, and I24. This work was funded by the Max Planck Society, Cancer Research UK (CRUK) (C375/A10976), the UK Medical Research Council (G9900061), and the Deutsche Forschungsgemeinschaft SFB 834 and EXC 115. D.d.T. was funded by a Marie Curie IEF fellowship (ID 274541). E.S. was supported by a CRUK travel grant (ref. C33663/A17200). E.C.B. was supported by a Wellcome Trust Doctoral Award, code RPSJ0. The Wellcome Trust Centre for Human Genetics (WTCHG) is supported by the Wellcome Trust (090532/Z/09/Z).

Accepted: October 2, 2014
Published: October 22, 2014

## REFERENCES

Aricescu, A.R., Lu, W., and Jones, E.Y. (2006). A time- and cost-efficient system for high-level protein production in mammalian cells. Acta Crystallogr. D Biol. Crystallogr. *62*, 1243–1250.

Bashaw, G.J., and Klein, R. (2010). Signaling from axon guidance receptors. Cold Spring Harb. Perspect. Biol. *2*, a001941.

Bella, J., Hindle, K.L., McEwan, P.A., and Lovell, S.C. (2008). The leucine-rich repeat structure. Cell. Mol. Life Sci. *65*, 2307–2333.

Bouvrée, K., Larrivée, B., Lv, X., Yuan, L., DeLafarge, B., Freitas, C., Mathivet, T., Bréant, C., Tessier-Lavigne, M., Bikfalvi, A., et al. (2008). Netrin-1 inhibits sprouting angiogenesis in developing avian embryos. Dev. Biol. *318*, 172–183.

Brasch, J., Harrison, O.J., Honig, B., and Shapiro, L. (2012). Thinking outside the cell: how cadherins drive adhesion. Trends Cell Biol. *22*, 299–310.

Calegari, F., Marzesco, A.-M., Kittler, R., Buchholz, F., and Huttner, W.B. (2004). Tissue-specific RNA interference in post-implantation mouse embryos using directional electroporation and whole embryo culture. Differentiation *72*, 92–102.

Cavallaro, U., and Dejana, E. (2011). Adhesion molecule signalling: not always a sticky business. Nat. Rev. Mol. Cell Biol. *12*, 189–197.

Chang, V.T., Crispin, M., Aricescu, A.R., Harvey, D.J., Nettleship, J.E., Fennelly, J.A., Yu, C., Boles, K.S., Evans, E.J., Stuart, D.I., et al. (2007). Glycoprotein structural genomics: solving the glycosylation problem. Structure *15*, 267–273.

Chen, X., Koh, E., Yoder, M., and Gumbiner, B.M. (2009). A protocadherin-cadherin-FLRT3 complex controls cell adhesion and morphogenesis. PLoS ONE *4*, e8411.

Chothia, C., and Jones, E.Y. (1997). The molecular structure of cell adhesion molecules. Annu. Rev. Biochem. *66*, 823–862.

Chung, K., and Deisseroth, K. (2013). CLARITY for mapping the nervous system. Nat. Methods *10*, 508–513.

Coles, C.H., Shen, Y., Tenney, A.P., Siebold, C., Sutton, G.C., Lu, W., Gallagher, J.T., Jones, E.Y., Flanagan, J.G., and Aricescu, A.R. (2011). Proteoglycan-specific molecular switch for RPTPσ clustering and neuronal extension. Science *332*, 484–488.

Cooper, J.A. (2013). Cell biology in neuroscience: mechanisms of cell migration in the nervous system. J. Cell Biol. *202*, 725–734.

Dahmann, C., Oates, A.C., and Brand, M. (2011). Boundary formation and maintenance in tissue development. Nat. Rev. Genet. *12*, 43–55.

Dimidschstein, J., Passante, L., Dufour, A., van den Ameele, J., Tiberi, L., Hrechdakian, T., Adams, R., Klein, R., Lie, D.C., Jossin, Y., and Vanderhaeghen, P. (2013). Ephrin-B1 controls the columnar distribution of cortical pyramidal neurons by restricting their tangential migration. Neuron *79*, 1123–1135.

Egea, J., Erlacher, C., Montanez, E., Burtscher, I., Yamagishi, S., Hess, M., Hampel, F., Sanchez, R., Rodriguez-Manzaneque, M.T., Bösl, M.R., et al. (2008). Genetic ablation of FLRT3 reveals a novel morphogenetic function for the anterior visceral endoderm in suppressing mesoderm differentiation. Genes Dev. *22*, 3349–3362.

Engelkamp, D. (2002). Cloning of three mouse Unc5 genes and their expression patterns at mid-gestation. Mech. Dev. *118*, 191–197.

Glaser, F., Pupko, T., Paz, I., Bell, R.E., Bechor-Shental, D., Martz, E., and Ben-Tal, N. (2003). ConSurf: identification of functional regions in proteins by surface-mapping of phylogenetic information. Bioinformatics *19*, 163–164.

Haines, B.P., Wheldon, L.M., Summerbell, D., Heath, J.K., and Rigby, P.W.J. (2006). Regulated expression of FLRT genes implies a functional role in the regulation of FGF signalling during mouse development. Dev. Biol. *297*, 14–25.

Hayashi, S., Lewis, P., Pevny, L., and McMahon, A.P. (2002). Efficient gene modulation in mouse epiblast using a Sox2Cre transgenic mouse strain. Mech. Dev. *119* (*Suppl 1*), S97–S101.

Hevner, R.F., Daza, R.A.M., Rubenstein, J.L.R., Stunnenberg, H., Olavarria, J.F., and Englund, C. (2003). Beyond laminar fate: toward a molecular classification of cortical projection/pyramidal neurons. Dev. Neurosci. *25*, 139–151.

Holm, L., and Rosenström, P. (2010). Dali server: conservation mapping in 3D. Nucleic Acids Res. *38*, W545–W549.

Kabsch, W. (1993). Automatic processing of rotation diffraction data from crystals of initially unknown symmetry and cell constants. J. Appl. Crystallogr. *26*, 795–800.

Kajander, T., Kuja-Panula, J., Rauvala, H., and Goldman, A. (2011). Crystal structure and role of glycans and dimerization in folding of neuronal leucine-rich repeat protein AMIGO-1. J. Mol. Biol. *413*, 1001–1015.

Karaulanov, E.E., Böttcher, R.T., and Niehrs, C. (2006). A role for fibronectin-leucine-rich transmembrane cell-surface proteins in homotypic cell adhesion. EMBO Rep. *7*, 283–290.

Karaulanov, E., Böttcher, R.T., Stannek, P., Wu, W., Rau, M., Ogata, S., Cho, K.W.Y., and Niehrs, C. (2009). Unc5B interacts with FLRT3 and Rnd1 to modulate cell adhesion in *Xenopus* embryos. PLoS ONE *4*, e5742.

Klein, R., and Kania, A. (2014). Ephrin signalling in the developing nervous system. Curr. Opin. Neurobiol. *27*, 16–24.

Koch, A.W., Mathivet, T., Larrivée, B., Tong, R.K., Kowalski, J., Pibouin-Fragner, L., Bouvrée, K., Stawicki, S., Nicholes, K., Rathore, N., et al. (2011). Robo4 maintains vessel integrity and inhibits angiogenesis by interacting with UNC5B. Dev. Cell *20*, 33–46.

Kolodkin, A.L., and Tessier-Lavigne, M. (2011). Mechanisms and molecules of neuronal wiring: a primer. Cold Spring Harb. Perspect. Biol. *3*, a001727.

Krissinel, E., and Henrick, K. (2004). Secondary-structure matching (SSM), a new tool for fast protein structure alignment in three dimensions. Acta Crystallogr. D Biol. Crystallogr. *60*, 2256–2268.

Lai Wing Sun, K., Correia, J.P., and Kennedy, T.E. (2011). Netrins: versatile extracellular cues with diverse functions. Development *138*, 2153–2169.

Larrivée, B., Freitas, C., Trombe, M., Lv, X., Delafarge, B., Yuan, L., Bouvrée, K., Bréant, C., Del Toro, R., Bréchot, N., et al. (2007). Activation of the UNC5B receptor by Netrin-1 inhibits sprouting angiogenesis. Genes Dev. *21*, 2433–2447.

Leyva-Díaz, E., del Toro, D., Menal, M.J., Cambray, S., Susín, R., Tessier-Lavigne, M., Klein, R., Egea, J., and López-Bendito, G. (2014). FLRT3 is a

Robo1-interacting protein that determines Netrin-1 attraction in developing axons. Curr. Biol. *24*, 494–508.

Lu, X., Le Noble, F., Yuan, L., Jiang, Q., De Lafarge, B., Sugiyama, D., Bréant, C., Claes, F., De Smet, F., Thomas, J.-L., et al. (2004). The netrin receptor UNC5B mediates guidance events controlling morphogenesis of the vascular system. Nature *432*, 179–186.

Luo, B.-H., Carman, C.V., and Springer, T.A. (2007). Structural basis of integrin regulation and signaling. Annu. Rev. Immunol. *25*, 619–647.

Maretto, S., Müller, P.-S., Aricescu, A.R., Cho, K.W.Y., Bikoff, E.K., and Robertson, E.J. (2008). Ventral closure, headfold fusion and definitive endoderm migration defects in mouse embryos lacking the fibronectin leucine-rich transmembrane protein FLRT3. Dev. Biol. *318*, 184–193.

Marquardt, T., Shirasaki, R., Ghosh, S., Andrews, S.E., Carter, N., Hunter, T., and Pfaff, S.L. (2005). Coexpressed EphA receptors and ephrin-A ligands mediate opposing actions on growth cone navigation from distinct membrane domains. Cell *121*, 127–139.

Müller, P.-S., Schulz, R., Maretto, S., Costello, I., Srinivas, S., Bikoff, E., and Robertson, E. (2011). The fibronectin leucine-rich repeat transmembrane protein Flrt2 is required in the epicardium to promote heart morphogenesis. Development *138*, 1297–1308.

Navankasattusas, S., Whitehead, K.J., Suli, A., Sorensen, L.K., Lim, A.H., Zhao, J., Park, K.W., Wythe, J.D., Thomas, K.R., Chien, C.-B., and Li, D.Y. (2008). The netrin receptor UNC5B promotes angiogenesis in specific vascular beds. Development *135*, 659–667.

Nieto, M., Monuki, E.S., Tang, H., Imitola, J., Haubst, N., Khoury, S.J., Cunningham, J., Gotz, M., and Walsh, C.A. (2004). Expression of Cux-1 and Cux-2 in the subventricular zone and upper layers II–IV of the cerebral cortex. J. Comp. Neurol. *479*, 168–180.

O'Sullivan, M.L., de Wit, J., Savas, J.N., Comoletti, D., Otto-Hitt, S., Yates, J.R., III, and Ghosh, A. (2012). FLRT proteins are endogenous latrophilin ligands and regulate excitatory synapse development. Neuron *73*, 903–910.

Rakic, P. (1988). Specification of cerebral cortical areas. Science *241*, 170–176.

Sawamiphak, S., Ritter, M., and Acker-Palmer, A. (2010). Preparation of retinal explant cultures to study ex vivo tip endothelial cell responses. Nat. Protoc. *5*, 1659–1665.

Scott, P.G., McEwan, P.A., Dodd, C.M., Bergmann, E.M., Bishop, P.N., and Bella, J. (2004). Crystal structure of the dimeric protein core of decorin, the archetypal small leucine-rich repeat proteoglycan. Proc. Natl. Acad. Sci. USA *101*, 15633–15638.

Scott, P.G., Dodd, C.M., Bergmann, E.M., Sheehan, J.K., and Bishop, P.N. (2006). Crystal structure of the biglycan dimer and evidence that dimerization is essential for folding and stability of class I small leucine-rich repeat proteoglycans. J. Biol. Chem. *281*, 13324–13332.

Seiradake, E., von Philipsborn, A.C., Henry, M., Fritz, M., Lortat-Jacob, H., Jamin, M., Hemrika, W., Bastmeyer, M., Cusack, S., and McCarthy, A.A. (2009). Structure and functional relevance of the Slit2 homodimerization domain. EMBO Rep. *10*, 736–741.

Seiradake, E., Harlos, K., Sutton, G., Aricescu, A.R., and Jones, E.Y. (2010). An extracellular steric seeding mechanism for Eph-ephrin signaling platform assembly. Nat. Struct. Mol. Biol. *17*, 398–402.

Solecki, D.J. (2012). Sticky situations: recent advances in control of cell adhesion during neuronal migration. Curr. Opin. Neurobiol. *22*, 791–798.

Torii, M., Hashimoto-Torii, K., Levitt, P., and Rakic, P. (2009). Integration of neuronal clones in the radial cortical columns by EphA and ephrin-A signalling. Nature *461*, 524–528.

Tronche, F., Kellendonk, C., Kretz, O., Gass, P., Anlag, K., Orban, P.C., Bock, R., Klein, R., and Schütz, G. (1999). Disruption of the glucocorticoid receptor gene in the nervous system results in reduced anxiety. Nat. Genet. *23*, 99–103.

Vielmetter, J., Stolze, B., Bonhoeffer, F., and Stuermer, C.A. (1990). In vitro assay to test differential substrate affinities of growing axons and migratory cells. Exp. Brain Res. *81*, 283–287.

Villar-Cerviño, V., Molano-Mazón, M., Catchpole, T., Valdeolmillos, M., Henkemeyer, M., Martínez, L.M., Borrell, V., and Marín, O. (2013). Contact repulsion controls the dispersion and final distribution of Cajal-Retzius cells. Neuron *77*, 457–471.

Wang, R., Wei, Z., Jin, H., Wu, H., Yu, C., Wen, W., Chan, L.-N., Wen, Z., and Zhang, M. (2009). Autoinhibition of UNC5b revealed by the cytoplasmic domain structure of the receptor. Mol. Cell *33*, 692–703.

Winter, G., Lobley, C.M.C., and Prince, S.M. (2013). Decision making in xia2. Acta Crystallogr. D Biol. Crystallogr. *69*, 1260–1273.

Yamagishi, S., Hampel, F., Hata, K., Del Toro, D., Schwark, M., Kvachnina, E., Bastmeyer, M., Yamashita, T., Tarabykin, V., Klein, R., and Egea, J. (2011). FLRT2 and FLRT3 act as repulsive guidance cues for Unc5-positive neurons. EMBO J. *30*, 2920–2933.